JOURNAL OF COMPUTATIONAL PHYSICS 122, 150–164 (1995)

A New Finite-Element Approach to Reconstruct a Bounded and Discontinuous Two-Dimensional Current Image from a Magnetic Field Map

SHAOFEN TAN, NESTOR SEPULVEDA, AND JOHN P. WIKSWO, JR.*

Living State Physics Group, Department of Physics and Astronomy, Nashville, Tennessee 37235

Received August 22, 1994; revised May 5, 1995

We introduce a new technique for constrained reconstructions of current distributions from magnetic field maps. By utilizing the finite element method, we can incorporate as much prior information as possible into the solution of the inverse problem, thereby improving the quality of a current image. In addition to constraining the current within the correct spatial region, boundary conditions can also be incorporated into the inverse solution. We also introduce a technique to avoid the difficulties in reconstruction of a discontinuous function, as occurs when electric current is injected into a conducting sample.

INTRODUCTION

In general, a two-dimensional current distribution has a current density $\mathbf{J}(x, y)$ distributed over the xy plane and produces a vector magnetic field $\mathbf{B}(x, y, z)$ above the distribution. A magnetometer can be scanned over the distribution to create a map of one or more components of the magnetic field [1, 2]. From this map, we wish to reconstruct the corresponding current distribution, i.e., to solve a two-dimensional magnetic inverse problem. Because of the typically ill-conditioned nature of the magnetic inverse problem, a variety of approaches has been developed, including spatial filtering [3], lead field analysis [4], and constrained reconstruction [5].

Our study [6] shows that if a current source has no actual boundary, the spatial filtering technique [3] provides an excellent way to estimate the current pattern. However, the spatial filtering technique [3] cannot readily incorporate any boundary conditions because of restrictions in the traditional algorithm for the inverse Fourier transformation. The lead field analysis introduced by Ioannides [4] provides a method to constrain the current-imaging space. However, because the lead field functions are defined over all space by using the *a priori* probability density function $w(r)$, lead field analysis can only incorporate a constraint condition, but not boundary conditions such as the specification that current can only flow tangentially to an insulating boundary. Second, the lead field interpolation functions are neither complete nor orthogonal, and this approach can only recover the components of the current distribution to which the pickup coil is sensitive. Therefore, the reconstructions are sensitive to the choice of the measurement locations and, hence, the lead field functions.

Constrained reconstruction [5] was originally proposed to solve the unbounded inverse Fourier transform problem. This method used a series of boxcar functions as the interpolation functions to represent the original function, so that the solution of the inverse Fourier transform is bounded. Because constrained reconstruction can eliminate the two drawbacks of lead field analysis, we extended this approach to solve a general integral equation which is often encountered in an inverse calculation. To have more flexibility in our mathematical modeling, we choose the finite element method which can readily incorporate *a priori* information about the object into the solution, such as the geometry of the current source, discontinuities, and boundary conditions.

In this paper, we first explain the basic idea of the finite element method and how it can be used to solve our current imaging problem. Then we apply this method to forward and inverse simulations. The results are compared to those obtained by using an unconstrained filtering technique. Finally, as an example that illustrates how the finite element method can help us solve more complex imaging problems, we use it to reconstruct the current distribution produced by point injection of current into a square plate and, in doing so, show how to overcome the effect of the current discontinuities at the current injection points.

THE FINITE ELEMENT METHOD (FEM)

According to the law of Biot-Savart, the z component of the magnetic field from a two-dimensional current distribution

* To whom editorial correspondence and reprint requests should be addressed.

0021-9991/95 $12.00

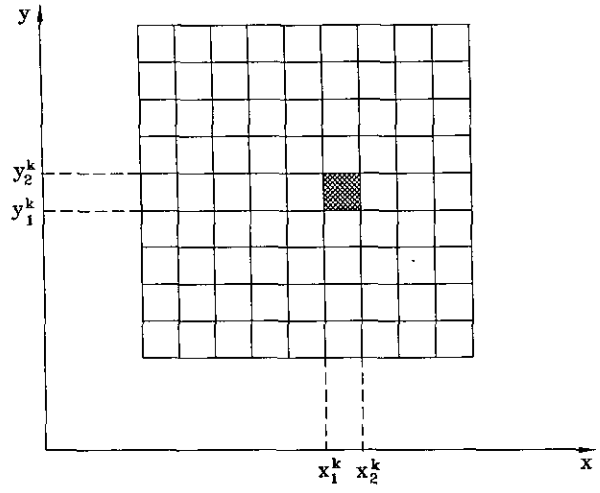

FIG. 1. The geometry of the two-dimensional system, showing the two-dimensional finite element grid. The current density $\mathbf{J}(x, y)$ is defined over the grid; the magnetic field is measured at a height z above the plane.

$\mathbf{J}(x', y')$ in the x'y' plane at $z' = 0$ obeys the equation

$$B_z(x, y, z) = \frac{\mu_0}{4\pi} \int \frac{[J_x(x', y')(y - y') - J_y(x', y')(x - x')]\, dx'dy'}{[(x - x')^2 + (y - y')^2 + z^2]^{3/2}}. \tag{1}$$

In order to reconstruct the current image $\mathbf{J}$ from the magnetic field data recorded in the xy plane at a height z above the current distribution, we section the current source space into a mesh of discrete elements as shown in Fig. 1. Inside each element we can represent the behavior of the current distributions in terms of the interpolation or shape functions as

$$\begin{aligned} J_x^k &= \sum_j \mathcal{J}_{xj}^k N_j^k(x', y') \\ J_y^k &= \sum_j \mathcal{J}_{yj}^k N_j^k(x', y'), \end{aligned} \tag{2}$$

where $\{N_j^k\}$ are the two-dimensional interpolation functions for the kth element, $\{\mathcal{J}_{xj}^k, \mathcal{J}_{yj}^k\}$ is a set of the nodal values that need to be determined, and j is the index for all interpolation functions in a single element. Substituting Eq. (2) into Eq. (1) and summing up all the elements, we obtain a set of linear equations

$$[B_{zi}] = \sum_k [A_{zi,xj}^k][\mathcal{J}_{xj}^k] - [A_{zi,yj}^k][\mathcal{J}_{yj}^k], \tag{3}$$

where the subscript i stands for the ith measurement and

$$A_{zi,xj}^k = \frac{\mu_0}{4\pi} \int\int_{(k)} \frac{N_j^k(x', y')(y_i - y')\, dx'dy'}{[(x_i - x')^2 + (y_i - y')^2 + z^2]^{3/2}} \tag{4}$$

$$A_{zi,yj}^k = \frac{\mu_0}{4\pi} \int\int_{(k)} \frac{N_j^k(x', y')(x_i - x')\, dx'dy'}{[(x_i - x')^2 + (y_i - y')^2 + z^2]^{3/2}}. \tag{5}$$

Because the z component of the magnetic field is related to both the x and y components of the current density, the solution of the above equations is, in general, highly singular and unstable. By incorporating the current continuity condition

$$\nabla \cdot \mathbf{J} = 0, \tag{6}$$

we can solve for the coefficients of the expansion functions, even if only the z component of the magnetic field is available.

The calculation of the matrices $A_{z,x}$, $A_{z,y}$, and their inverses consumes much computer time. Fortunately the matrices $A_{z,x}$ and $A_{z,y}$ only depend on the geometry of the finite element mesh and the measurement arrangement. Thus, if the set of positions of the sample relative to the pickup coil remains unchanged, the coefficient matrices $A_{z,x}$ and $A_{z,y}$ of the linear equation will need to be calculated only once. We can compute and save the matrices $A_{z,x}$ and $A_{z,y}$ for different experimental setups and recall them as required. Once the matrices $A_{z,x}$ and $A_{z,y}$ are calculated, it only takes a few minutes to obtain the solutions on a modest workstation.

We can derive the reconstruction equations for the other two components of the magnetic field, B_x and B_y, by the same approach. According to the law of Biot-Savart, the x and y components of the magnetic fields are related to the current density by

$$\begin{aligned} B_x(x, y, z) &= \frac{\mu_0}{4\pi} \int \frac{J_y(x', y')z\, dx'dy'}{[(x - x')^2 + (y - y')^2 + z^2]^{3/2}} \\ B_y(x, y, z) &= \frac{\mu_0}{4\pi} \int \frac{-J_x(x', y')z\, dx'dy'}{[(x - x')^2 + (y - y')^2 + z^2]^{3/2}}, \end{aligned} \tag{7}$$

and the corresponding matrix equations about the nodal values are

$$[B_{xi}] = \sum_k [A_{xi,yj}^k][\mathcal{J}_{yj}^k] \tag{8}$$

$$[B_{yi}] = \sum_k [A_{yi,xj}^k][\mathcal{J}_{xj}^k], \tag{9}$$

where

$$\begin{aligned} A_{xi,yj}^k &= \frac{\mu_0}{4\pi} \int\int_{(k)} \frac{N_j^k(x', y')z\, dx'dy'}{[(x_i - x')^2 + (y_i - y')^2 + z^2]^{3/2}} \\ A_{yi,xj}^k &= \frac{\mu_0}{4\pi} \int\int_{(k)} \frac{N_j^k(x', y')z\, dx'dy'}{[(x_i - x')^2 + (y_i - y')^2 + z^2]^{3/2}}. \end{aligned} \tag{10}$$

Note that the matrices $A_{x,y}$ and $A_{y,x}$ are identical to each other except they have the opposite sign. From Eqs. (8) and (9), we

see that one tangential component of the magnetic field is related only to another component of the current density. By incorporating the continuity condition Eq. (6), it is still possible to reconstruct the whole current pattern from either the x or y components of the magnetic field. Because the above equations separate J_x and J_y, the dimension of the matrix $A_{x,y}$ for Eq. (7) reduces to one-half of the matrix $A_{z,x/y}$ in Eq. (3), and the computational time will be reduced. If both the x and y components of the magnetic field are available as the input data, then we can solve for J_x and J_y independently, without the aid of the continuity condition. This is especially useful when the current is not continuous everywhere in the plane and the expression for the current continuity equation cannot be determined experimentally.

However, the linear equations are usually either singular or numerically close to singular, thereby preventing a simple inversion of the corresponding matrix. Singular value decomposition (SVD) [7] is a powerful technique used to deal with matrices that are either singular or numerically close to singular. The basic idea of SVD is that any $M \times N$ matrix A can be written as the product of an $M \times N$ matrix U, an $N \times N$ diagonal matrix W with positive or zero elements (λ_j), and the transpose of an $N \times N$ matrix V, i.e.,

$$A = U \cdot [\mathrm{diag}(\lambda_j)] \cdot V^{\mathrm{T}}. \tag{11}$$

The inverse of matrix A is

$$A^{-1} = V \cdot [\mathrm{diag}(1/\lambda_j)] \cdot U^{\mathrm{T}}. \tag{12}$$

As long as λ_j is neither zero nor so small as to have an excessively large reciprocal value (which would make the inverted matrix dominated by the roundoff errors), Eq. (12) will give the optimal inversion of the matrix in the least-squares sense. Furthermore, if we constrain the current sources within the correct boundary and impose the correct boundary conditions on the current density, then the ill-conditioned matrices in the linear equations (3), (8), and (9) will be improved. In the next section, we simulate two types of current imaging problems: one with a continuous current distribution and the other with discontinuous current sources.

SIMULATIONS

Continuous Two-Dimensional Current Distribution

For simplicity, a bilinear finite element is used, and its interpolation function has the form [8]

$$N_j^k(x, y) = a_j^k + b_j^k x + c_j^k y + d_j^k xy, \tag{13}$$

where a_j^k, b_j^k, c_j^k, and d_j^k are the parameters specific to the kth element. For convenience, we usually rewrite this interpolation function in the natural coordinate system. If we denote x_1^k, x_2^k, y_1^k, y_2^k as the coordinates for the kth element as shown in Fig. 1, then the interpolation functions can be written as

$$N_j^k(\xi, \eta) = \begin{cases} \frac{1}{4}(1 \pm \xi)(1 \pm \eta) & \text{if } \xi, \eta \in [-1, 1], j = 1, 2, 3, 4, \\ 0 & \text{otherwise}, j = 1, 2, 3, 4, \end{cases} \tag{14}$$

with

$$\begin{aligned} \xi &= \frac{x - x_c^k}{a^k} \\ \eta &= \frac{y - y_c^k}{b^k} \\ a^k &= \frac{x_2^k - x_1^k}{2} \\ b^k &= \frac{y_2^k - y_1^k}{2} \\ x_c^k &= \frac{x_1^k + x_2^k}{2} \\ y_c^k &= \frac{y_1^k + y_2^k}{2}. \end{aligned} \tag{15}$$

Inside the kth element, the current distribution $\mathbf{J}$ can be expressed as

$$\begin{aligned} J_x^k &= \mathcal{J}_{x1}^k N_1^k + \mathcal{J}_{x2}^k N_2^k + \mathcal{J}_{x3}^k N_3^k + \mathcal{J}_{x4}^k N_4^k \\ J_y^k &= \mathcal{J}_{y1}^k N_1^k + \mathcal{J}_{y2}^k N_2^k + \mathcal{J}_{y3}^k N_3^k + \mathcal{J}_{y4}^k N_4^k. \end{aligned} \tag{16}$$

Explicitly rewriting the continuity condition (Eq. (6)) in the two-dimensional natural coordinate system, we obtain

$$\frac{\partial J_x}{\partial \xi}\frac{\partial \xi}{\partial x} + \frac{\partial J_y}{\partial \eta}\frac{\partial \eta}{\partial y} = 0. \tag{17}$$

Substituting Eq. (16) into the above equation and sorting the coefficients by the order of the polynomial, we obtain a polynomial expression for the continuity equation

$$\begin{aligned} &\frac{1}{a^k}(-\mathcal{J}_{x1}^k + \mathcal{J}_{x2}^k - \mathcal{J}_{x3}^k + \mathcal{J}_{x4}^k) \\ &\quad + \frac{1}{b^k}(-\mathcal{J}_{y1}^k - \mathcal{J}_{y2}^k + \mathcal{J}_{y3}^k + \mathcal{J}_{y4}^k) \\ &\quad + \frac{1}{a^k}(\mathcal{J}_{x1}^k - \mathcal{J}_{x2}^k - \mathcal{J}_{x3}^k + \mathcal{J}_{x4}^k)\eta \\ &\quad + \frac{1}{b^k}(\mathcal{J}_{y1}^k - \mathcal{J}_{y2}^k - \mathcal{J}_{y3}^k + \mathcal{J}_{y4}^k)\xi = 0. \end{aligned} \tag{18}$$

Since the coordinates ξ and η are independent of each other, each term of the polynomial must be individually zero to assure that the continuity condition is satisfied in every element. Thus, we obtain a set of equations governing the coefficients $\mathcal{J}^k_{xj}$ and $\mathcal{J}^k_{yj}$:

$$\begin{aligned}
&\frac{1}{a^k}(-\mathcal{J}^k_{x1} + \mathcal{J}^k_{x2} - \mathcal{J}^k_{x3} + \mathcal{J}^k_{x4}) \\
&\quad + \frac{1}{b^k}(-\mathcal{J}^k_{y1} - \mathcal{J}^k_{y2} + \mathcal{J}^k_{y3} + \mathcal{J}^k_{y4}) = 0 \\
&(\mathcal{J}^k_{x1} - \mathcal{J}^k_{x2} - \mathcal{J}^k_{x3} + \mathcal{J}^k_{x4}) = 0 \\
&(\mathcal{J}^k_{y1} - \mathcal{J}^k_{y2} - \mathcal{J}^k_{y3} + \mathcal{J}^k_{y4}) = 0.
\end{aligned} \tag{19}$$

By incorporating the continuity condition (Eq. (19)) into one of the reconstruction equations (Eqs. (3), (8), or (9)), we can obtain the images of the current density using only one component of the magnetic field.

Since the finite element method can deal with each individual element, any kind of boundary condition is easy to incorporate into the solution. For instance, a bounded current source usually will not allow current to flow out of the edge, which means that the boundary condition is

$$\mathbf{J} \cdot \hat{n} = 0. \tag{20}$$

Because the interpolation functions in the finite element method are designed so that the nodal values are simply the current densities at the nodes, if the nodal values of the current component normal to the edge are zero, then this boundary condition is satisfied along that edge.

In order to compare quantitatively a current image with the original distribution, we define a mean square deviation (MSD),

$$\mathrm{MSD}_J = \frac{\int |\mathbf{J}(\mathbf{x}, \mathbf{y}) - \mathbf{J}_{\mathrm{image}}(\mathbf{x}, \mathbf{y})|^2 \, dxdy}{\int |\mathbf{J}(\mathbf{x}, \mathbf{y})|^2 \, dxdy}. \tag{21}$$

When the original data is not available, the MSD is defined as

$$\mathrm{MSD}_B = \frac{\int [B_z(x, y, z_0) - B_z^{\mathrm{fit}}(x, y, z_0)]^2 \, dxdy}{\int B_z^2(x, y, z_0) \, dxdy}. \tag{22}$$

As a simple example of this approach, we consider a 11.7 mm × 12.6 mm current loop as shown in Fig. 2. We calculate the corresponding magnetic field measured at $z = 1.5$ mm for x, y, and z components shown in Figs. 4a, 4b, and 4c, respectively. The magnetic field is sampled over a 25 mm × 25 mm area with 26 by 26 discrete points.

Assuming we have prior knowledge about the current source, which contains the information about the geometry of the current source and the boundary condition of Eq. (20), we construct the mesh shown in Fig. 3 to form the current space. The images

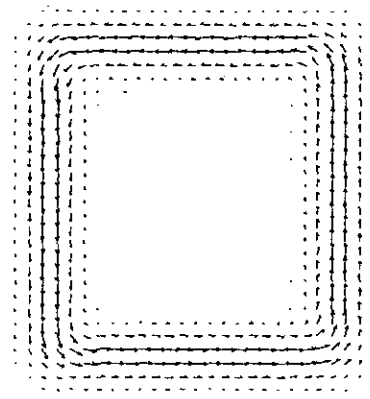

FIG. 2. The simulated current source used to test the reconstruction algorithm.

in Figs. 4b, 4d, 4f show the current patterns reconstructed individually by the finite element method from the magnetic fields in Figs. 4a, 4c, and 4e, respectively. The MSDs for each reconstruction from the x, y, and z components of the magnetic field have been calculated and are listed in the caption of Fig. 4. Besides using the MSD to measure the quality of an image, we also plot cross sections of the current density and compare them to the original data (see Fig. 5). We observe that the image with the larger MSD has greater distortion from the original than one with the smaller MSD. Because the current pattern is not exactly square, which means that B_x is not totally symmetrical to B_y, the MSD for the reconstruction from B_x will not be equal to that from B_y.

Since the normal component of the magnetic field is typically measured by SQUID magnetometers, we will concentrate on the algorithm using the z component of the magnetic field as the only input data and compare it with the filtering technique. Figure 6a shows the z component of the magnetic field data used in the filtering technique to reconstruct the current pattern shown in Fig. 6b; the MSD of 0.0021 is better than the MSD for the reconstruction by the FEM. Considering that the filtering technique uses many more data points (60 by 60 sampling in

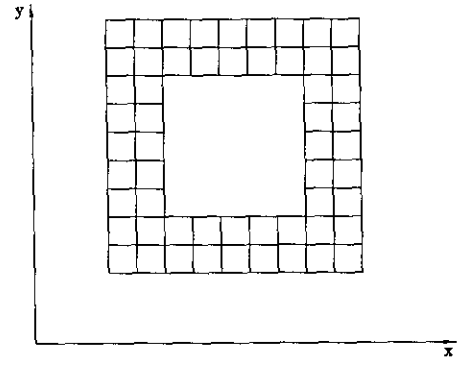

FIG. 3. The grid used to section the current space corresponding to Fig. 2.

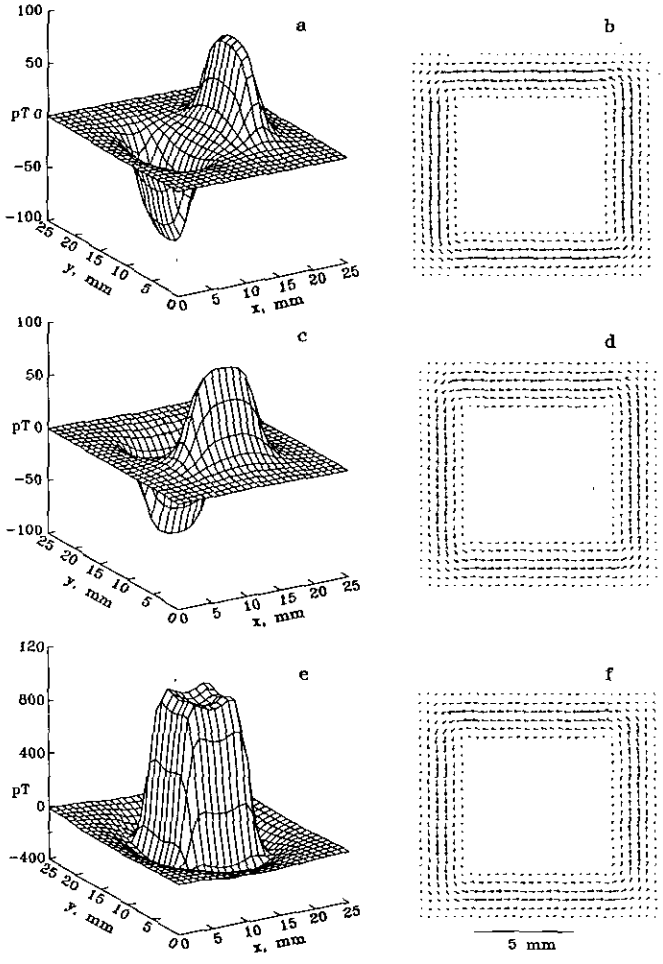

FIG. 4. The magnetic field components produced by the current pattern shown in Fig. 2 at $z = 1.5$ mm without noise and the corresponding reconstructions by FEM: (a) and (b) B_x and its image with MSD of 0.056; (c) and (d) B_y and its image with MSD of 0.029; (e) and (f) B_z and its image with MSD of 0.026.

contrast to 26 by 26), its image quality should be higher than that obtained by the finite element method. Due to the size of the matrix in the finite element method, the number of data points is limited by the memory capacity in our computer. In an ideal case, when no noise is present in the data and the data is recorded very close to the current source, the filtering technique has the advantages of dealing with a large amount of data quickly and obtaining an excellent result. However, even a small amount of noise will reduce severely the quality of the image produced by the filtering technique, producing current noise over the entire image plane, while the finite element method controls the effects of the noise in the magnetic field by limiting the current within the correct boundary.

To simulate the experimental data, noise levels of 5% (SNR = 20) are added to the ideal magnetic field data. Figures 7(a, b) show the results of the filtering technique and the finite element method, respectively. The MSD for the result from the filtering technique (Fig. 7a) increases from 0.00218 to 0.133, which means that even a 5% noise level will degrade the quality of the image 60 times, as compared to the reconstruction from

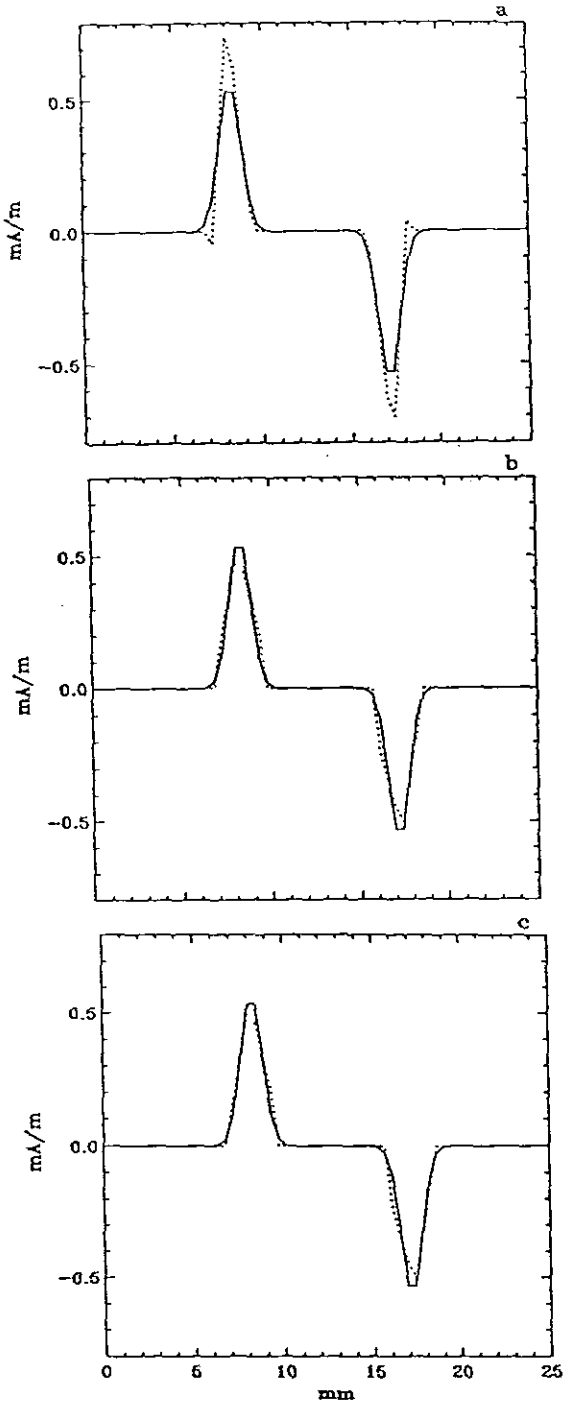

FIG. 5. The cross sections of the current images calculated from (a) B_x; (c) B_y; (e) B_z in Fig. 4. The solid lines are the original current densities, and the dotted lines are the reconstructions.

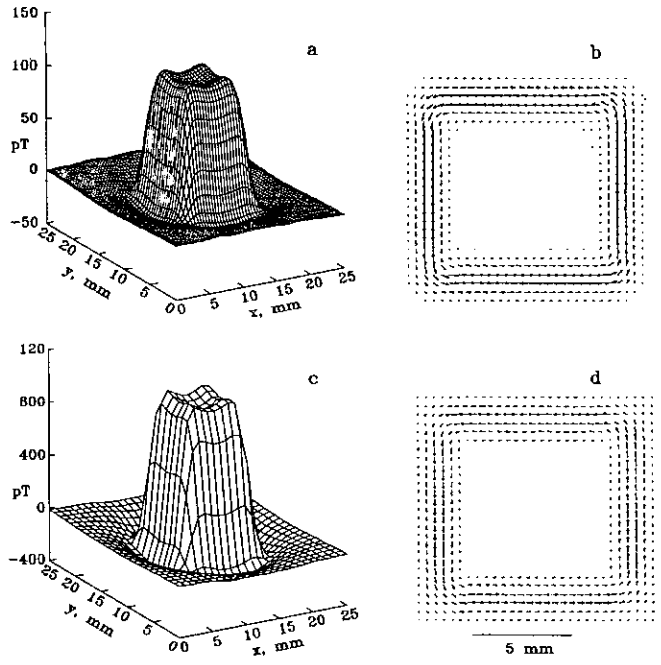

FIG. 6. The comparison between the unconstrained filtering technique (FT) and the constrained finite element method (FEM) from noise-free data: (a) The magnetic field (B_z) produced by the current pattern of Fig. 2 at z = 1.5 mm with no noise and sampling of 60 by 60; (b) the reconstructions by the FT; (c) the same magnetic field data as shown in Fig. 6a with sampling of 26 by 26; (d) the reconstructions by the FEM.

the noise-free data. In contrast, the MSD for the finite element method (Fig. 7b) only increases from 0.026 to 0.040. With the aid of prior knowledge about the current source, the intrinsic singularity of the inverse calculation is reduced, and the quality of the image is enhanced. The incorporation of the prior knowledge of the current source in the finite element method can also control the instability of the filtering technique due to the large coil-to-source distance. When the magnetic field data is recorded 3.0 mm away from the current sources and without any noise in the input data, the quality of the image calculated by the filtering technique (Fig. 8a) decreases from a MSD of 0.0022 to one of 0.077, which is 35 times worse than that using the input data recorded at 1.5 mm. Under the same conditions, the result of the finite element method (Fig. 8b) remains very close to the original one, while using many fewer input data points than the filtering technique. The MSD is only 0.0267, which is 29% of the result for the filtering technique.

Considering an extreme case where the magnetic field data is measured at z = 3.0 mm with a 20% noise level (SNR = 5), the advantage of using prior knowledge is distinctly shown in the results. Figure 9a shows the result of the filtering technique with a MSD of 0.42. For the finite element method, the result is shown in Fig. 9b with a MSD of 0.12. The comparison between the two techniques is summarized in Table I.

Discontinuous Two-Dimensional Current Sources

In the quasi-static state, current must be continuous in the whole space. When we are only interested in the object studied, we often encounter a discontinuous situation where the current is flowing into the object at one place and flowing out at another. An excellent example of a discontinuous, two-dimensional current distribution is shown in Fig. 10; a 24.5 mm by 24.5 mm homogeneous conducting plate has two electrodes located at (2.25 mm, 12.25 mm) and (22.25 mm, 12.25 mm) that inject and remove, respectively, a 1 mA current into the conducting plate via perpendicular wires. Because the wires are perpendicular to the plane, as is the measured component of the magnetic field, the current in the wires does not contribute to the magnetic map.

The current distribution in the plate is a classic electrostatic problem in which the electric potential ϕ of the conducting plate obeys the two-dimensional Poisson equation

$$\nabla^2\phi = V\delta(\mathbf{r} - \mathbf{r}_1) - V\delta(\mathbf{r} - \mathbf{r}_2), \tag{23}$$

with the boundary condition

$$\nabla\phi \cdot \hat{n} = 0, \tag{24}$$

where the coefficient V in Eq. (23) depends on the magnitude of the injected current and the resistance of the conducting plate, and $\mathbf{r}_1$ and $\mathbf{r}_2$ are the positions of the electrodes. After the electric potential ϕ is obtained from Poisson's equation, we can determine the current distribution in the conducting plate by taking the derivative of the potential with respect to x and y. Since we are examining a conducting plate of finite size, we can readily obtain the numerical solution to Eq. (23) by using the finite element technique, with the result shown in Fig. 11a. The corresponding magnetic field as would be measured at 1.5 mm above the plate is shown in Fig. 11b. From the calculated magnetic field data, we will try to reconstruct the current image of the original current distribution by, first, the filtering technique and, then, the finite element method.

Figure 12b shows the current image using the unconstrained filtering technique. The unacceptable spreading of the image as compared to the original distribution in Fig. 12a is obvious. We can avoid this by utilizing our knowledge of the geometry to constrain the current patterns. As before, we first establish a mesh according to the geometry of the object. Second, by substituting the boundary conditions into the finite element equations, we can further reduce the singularity and force the solution to closely approximate the real current distribution. The continuity condition becomes

$$\nabla \cdot \mathbf{J} = V\delta(\mathbf{r} - \mathbf{r}_1) - V\delta(\mathbf{r} - \mathbf{r}_2). \tag{25}$$

For the continuous elements, the continuity condition expressed in the finite element interpolation functions has the same form

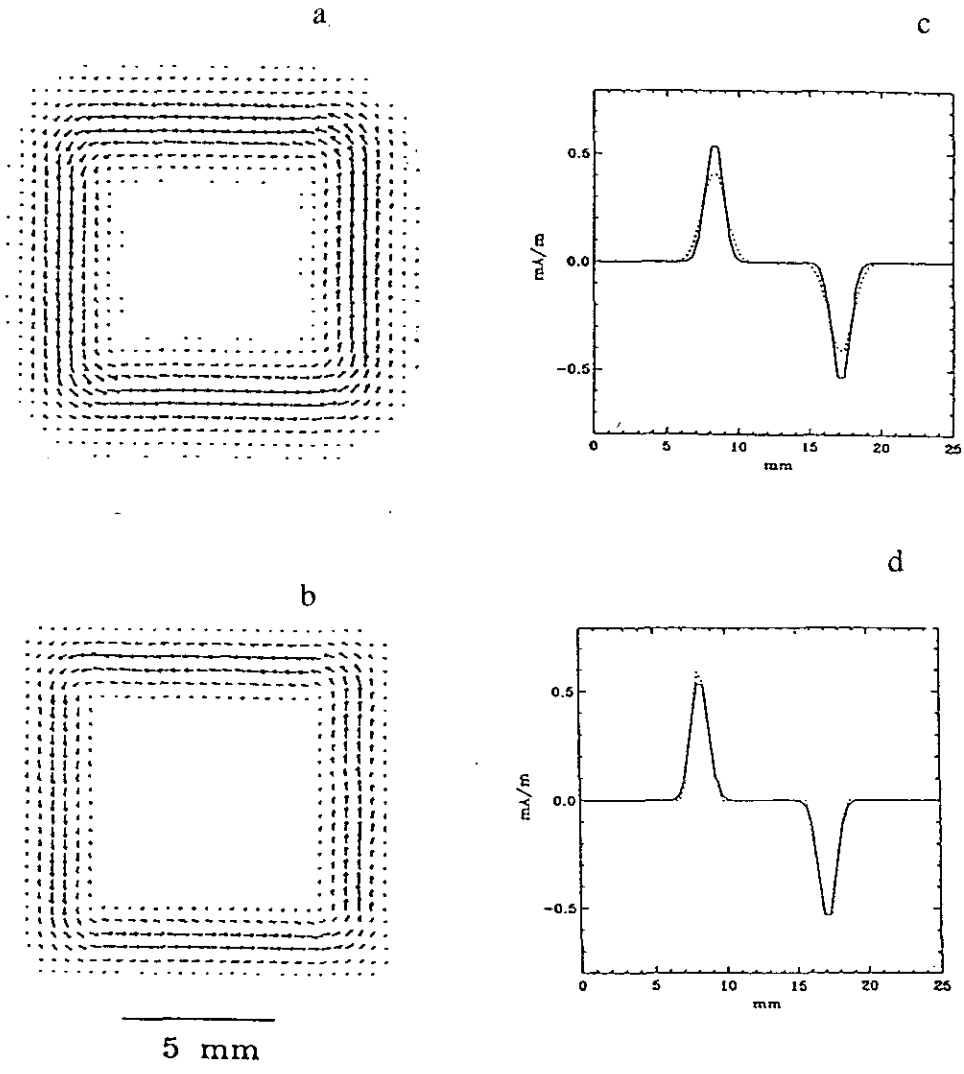

FIG. 7. The reconstructions by the FT and the FEM at $z = 1.5$ mm with SNR = 20. The magnetic field is calculated at $z = 1.5$ mm and the SNR = 20: (a) by the FT; (b) by the FEM; (c) the cross section of J_x by the FT; (d) the cross section of J_x by the FEM.

as was expressed in Eq. (19). For the element containing the discontinuous points, the continuity equation becomes

$$\frac{1}{b^k}(-\mathcal{J}^k_{x1} + \mathcal{J}^k_{x2} - \mathcal{J}^k_{x3} + \mathcal{J}^k_{x4}) + \frac{1}{a^k}(-\mathcal{J}^k_{y1} - \mathcal{J}^k_{y2} + \mathcal{J}^k_{y3} + \mathcal{J}^k_{y4}) = \pm A$$

$$(\mathcal{J}^k_{x1} - \mathcal{J}^k_{x2} - \mathcal{J}^k_{x3} + \mathcal{J}^k_{x4}) = 0$$

$$(\mathcal{J}^k_{y1} - \mathcal{J}^k_{y2} - \mathcal{J}^k_{y3} + \mathcal{J}^k_{y4}) = 0.$$

By using the SVD algorithm, we find the most likely solution for this overdetermined system. The image of the current source is shown in Fig. 13a and its MSD is 0.13. From the corresponding cross sections in Fig. 14, we notice that the current density around the injecting points is more distorted than those in other positions.

We know that the finite element interpolation function can interpolate the continuous functions to any degree of approximation, depending on the orders of the elements. Since the interpolation functions are continuous, they are not well suited to approximate a discontinuous function. The usual solution to this problem is to refine the mesh near the discontinuity imposed by the current-injecting electrodes, so that a large number of small elements (either 3-node triangular elements or higher-order quadrilateral ones) are concentrated in regions of high potential gradients. Depending upon the accuracy required near the electrodes, the total number of elements in the problem can easily be doubled or tripled. In our case, for which we are interested in inverting the finite-element matrix to obtain an inverse image, this would increase the size and complexity of

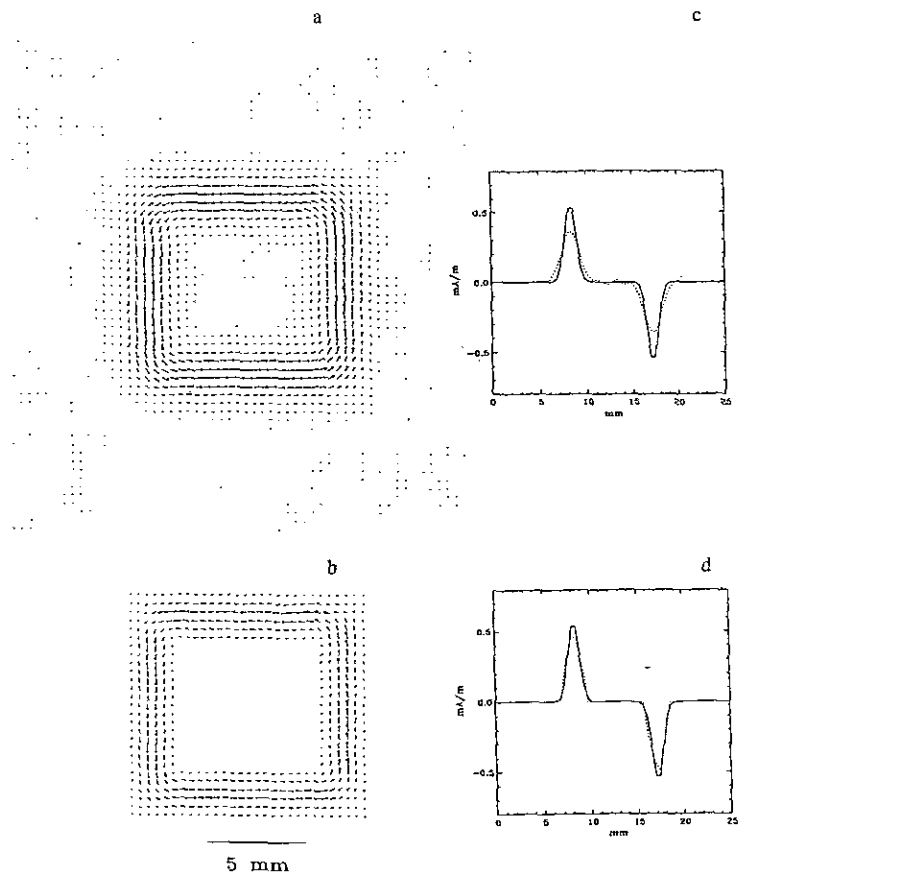

FIG. 8. The reconstructions by the FT and the FEM at $z = 3.0$ mm with SNR = ∞. The magnetic field is calculated at $z = 3.0$ mm and the SNR = ∞: (a) by the FT; (b) by the FEM; (c) the cross section of J_x by the FT; (d) the cross section of J_x by the FEM.

the matrix to be inverted by singular value decomposition. We have devised an alternative approach that allows us to maintain a uniform, rectangular mesh. We separate the current distribution into two parts: one that is related to the divergent component $\mathbf{J}_d$ and the other that is the divergence-free component $\mathbf{J}_c$, i.e.,

$$\mathbf{J} = \mathbf{J}_d + \mathbf{J}_c. \tag{27}$$

The divergent part can be expressed by some known discontinuous functions $\mathbf{J}_d(\mathbf{r})$ whose forms depend on the individual problem. The divergence-free part $\mathbf{J}_c$ is chosen by the finite element method so that the summation of the two parts produces the same magnetic field as measured and also satisfies the correct boundary condition.

For the current pattern discussed in this paper, the choice for the divergent part is obviously the analytical solution for an infinite, two-dimensional plate with two electrodes located at the same positions, whose potential is given by [9]

$$\begin{aligned}\phi = {} & V \log \sqrt{(x - x_1)^2 + (y - y_1)^2} \\ & - V \log \sqrt{(x - x_2)^2 + (y - y_2)^2}.\end{aligned} \tag{28}$$

The corresponding current density can be calculated as

$$\begin{aligned} J_{dx} &= \frac{\partial \phi}{\partial x} \\ &= \frac{V \cdot (x - x_1)}{(x - x_1)^2 + (y - y_1)^2} - \frac{V \cdot (x - x_2)}{(x - x_2)^2 + (y - y_2)^2} \end{aligned} \tag{29}$$

$$\begin{aligned} J_{dy} &= \frac{\partial \phi}{\partial y} \\ &= \frac{V \cdot (y - y_1)}{(x - x_1)^2 + (y - y_1)^2} - \frac{V \cdot (y - y_2)}{(x - x_2)^2 + (y - y_2)^2}. \end{aligned} \tag{30}$$

Then the deconvolution problem becomes that of trying to find the divergence-free component J_c so that the total current J will produce the correct magnetic field while satisfying both the boundary condition,

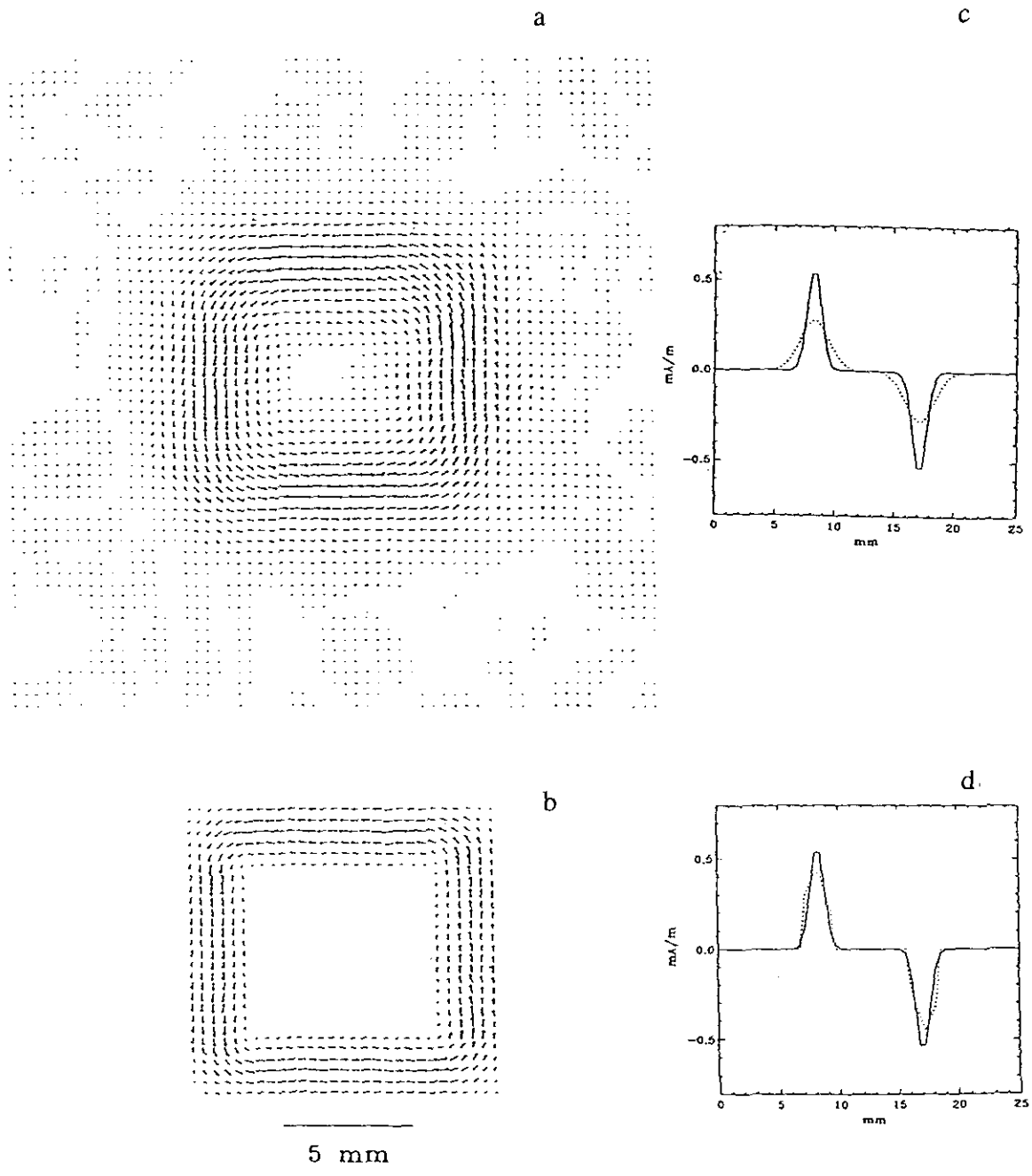

FIG. 9. The reconstructions by the FT and the FEM at $z = 3.0$ mm with SNR = 5. The magnetic field is calculated at $z = 3.0$ mm and the SNR = 5: (a) by the FT; (b) by the FEM; (c) the cross section of J_x by the FT; (d) the cross section of J_x by the FEM.

TABLE I

The Comparison of FT and FEM for the Continuous Current Pattern

z (mm)	1.5	1.5	3.0	3.0
SNR	∞	20	∞	5
MSD for FT	0.0021	0.13	0.077	0.42
MSD for FEM	0.026	0.040	0.027	0.12

$$(\mathbf{J}_d + \mathbf{J}_c) \cdot \hat{n} = 0, \tag{31}$$

and also the continuity condition,

$$\nabla \cdot \mathbf{J}_d = V\delta(\mathbf{r} - \mathbf{r}_1) - V\delta(\mathbf{r} - \mathbf{r}_2) \tag{32}$$

$$\nabla \cdot \mathbf{J}_c = 0. \tag{33}$$

Figure 13b shows the results of deconvolution, for which

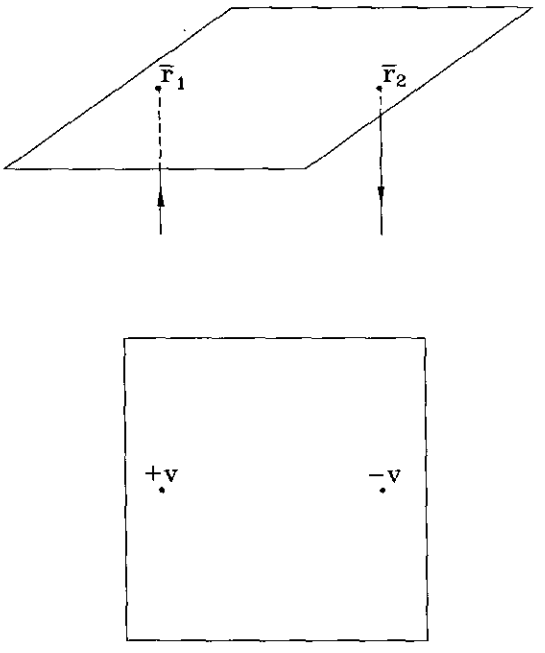

FIG. 10. A homogeneous conducting plate with two electrodes located at $\mathbf{r}_1$ and $\mathbf{r}_2$.

the MSD is reduced to 0.068. Comparing the result from the filtering technique with the original current image (Fig. 12a), we see that the corresponding MSD for the filtering techniques of 0.44 is seven times worse than the results of the two-part finite element method.

In the particular example we present, we only measure B_z and, hence, we do need *a priori* knowledge of the location of the current injection electrodes, since those are the points where there is a discontinuity of the current in the plane and, hence, are where Eq. (6), required for the solutions of Eqs. (4) and (5), is not valid. To not know the location of the current injection points presents an added experimental complication, in that measurement of B_z alone is insufficient to obtain an exact inverse solution. As discussed earlier, this restraint could be relaxed by measuring the B_x and B_y field components. If *a priori* knowledge of the current injection sites and the analytical solution were not used, it may be possible to use adaptive mesh refinement techniques to minimize the effect of the discontinuities, but then it would be necessary to devise tests for their presence. As the goal of the present study was to devise techniques to incorporate as much *a priori* knowledge into the inverse solution as is possible, we find the combined finite-element/analytical approach ideally suited to incorporate both the edge boundary condition (Eq. (20)) and that for point injection of current (Eq. (25)) while using a simple finite element mesh. Both approaches can be applied to planar samples of irregular shape.

THE DETECTION OF THE INHOMOGENEOUS CONDUCTIVITY OF TWO-DIMENSIONAL OBJECTS

Once we have reconstructed the current image from the magnetic field data, we can use the current image to obtain information about the object that is not readily apparent in the magnetic field data. For the z component of the magnetic field, we had that

$$B_z(x, y) = \frac{\mu_0}{4\pi} \int \frac{[J_x(x', y')(y - y') - J_y(x', y')(x - x')]\, dx'\, dy'}{[(x - x')^2 + (y - y')^2 + z^2]^{3/2}}. \quad (34)$$

By using a partial integration, we can rewrite the above equation as [10]

$$B_z(\mathbf{r}) = \frac{\mu_0}{4\pi} \oint \frac{\mathbf{J}(\mathbf{r}') \cdot \mathbf{dl}'}{|\mathbf{r} - \mathbf{r}'|} - \frac{\mu_0}{4\pi} \int \frac{(\nabla \times \mathbf{J}(\mathbf{r}'))_z\, dx'\, dy'}{|\mathbf{r} - \mathbf{r}'|}. \quad (35)$$

According to Ohm's law,

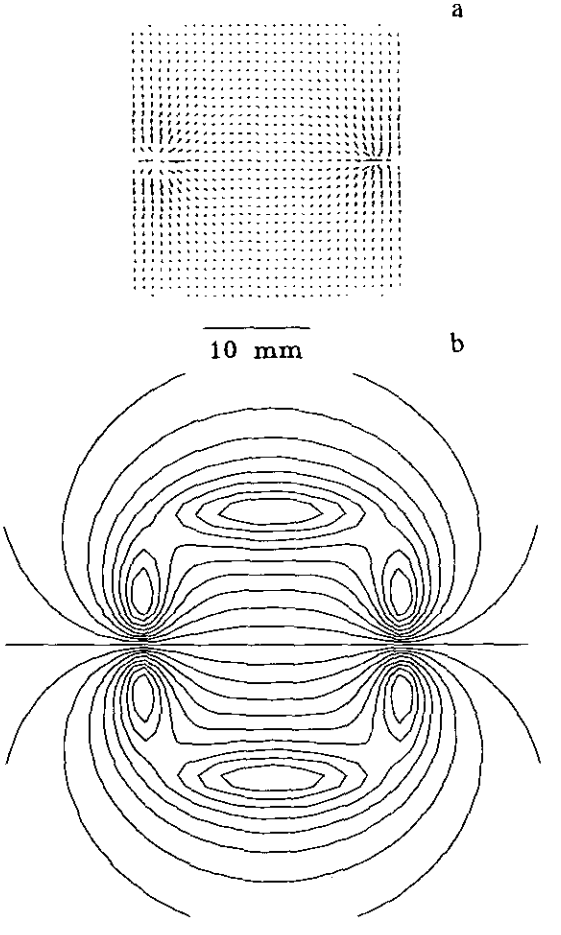

FIG. 11. The test current pattern for the FEM and the FT: (a) The original current distribution of the conducting plate shown in Fig. 10; (b) the magnetic field B_z calculated at $z = 1.5$ mm without any noise (1.3 nT contours).

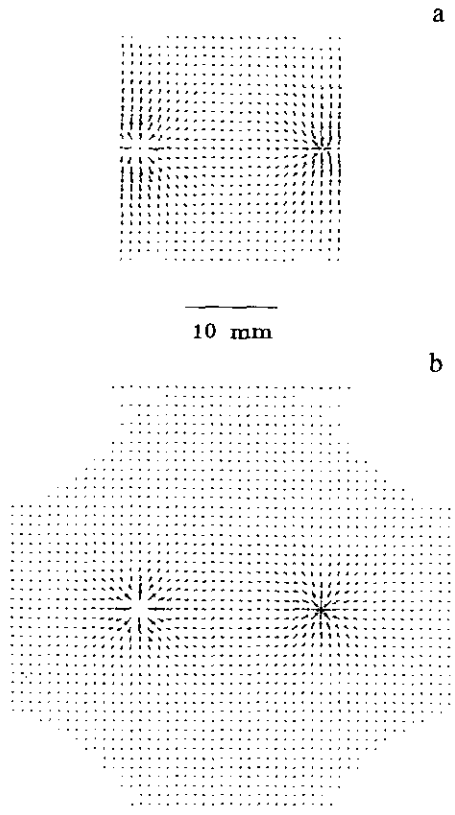

FIG. 12. The comparison of the original pattern and the reconstruction by the filtering technique (FT): (a) The original current distribution; (b) the reconstruction by the FT, with MSD of 0.44.

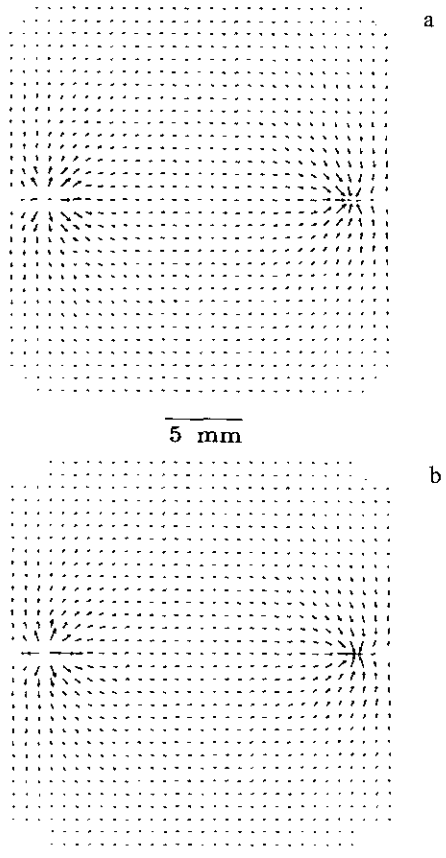

FIG. 13. The reconstructions by the FEM for the discontinuous current distribution: (a) By the regular FEM, with MSD of 0.13; (b) by the adapted FEM, with MSD of 0.06.

$$\mathbf{J} = \sigma \nabla \phi \tag{36}$$

and

$$\begin{aligned} \nabla \times \mathbf{J} &= \nabla \times (\sigma \nabla \phi) \\ &= \nabla \sigma \times \nabla \phi \\ &= -\nabla \times (\phi \nabla \sigma), \end{aligned} \tag{37}$$

so that we can rewrite Eq. (35) as

$$\begin{aligned} B_z(\mathbf{r}) = &\frac{\mu_0}{4\pi} \oint_s \frac{\mathbf{J}(\mathbf{r}') \cdot \mathbf{dl}'}{|\mathbf{r} - \mathbf{r}'|} \\ &+ \frac{\mu_0}{4\pi} \int \frac{(\phi(\mathbf{r}')\, \nabla' \sigma \times \mathbf{r}')_z \, dx'\, dy'}{|\mathbf{r} - \mathbf{r}'|}. \end{aligned} \tag{38}$$

If $\nabla \sigma = 0$, which means the conductivity of the object is homogeneous and isotropic, then the magnetic field only depends on the current at the edge

$$B_z(\mathbf{r}) = \frac{\mu_0}{4\pi} \oint_s \frac{\mathbf{J}(\mathbf{r}') \cdot \mathbf{dl}'}{|\mathbf{r} - \mathbf{r}'|}. \tag{39}$$

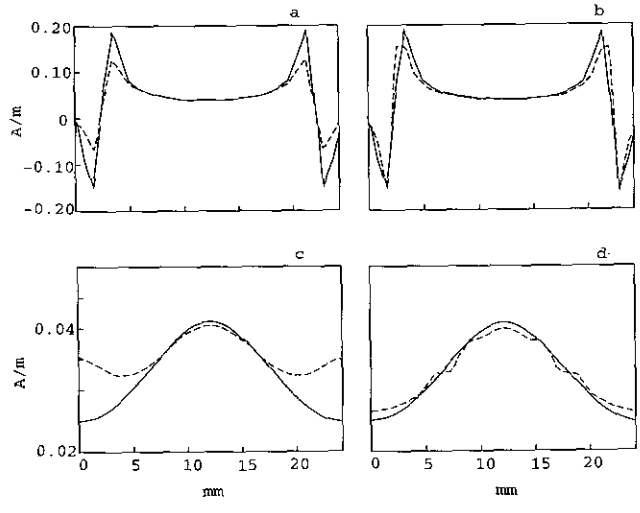

FIG. 14. The cross sections in two positions of the reconstructions in Fig. 13. The solid line represents the original current pattern and the dotted line is for the reconstruction: (a) and (b) by the regular FEM; (c) and (d) by the adapted FEM; (a) and (c) the cross section at $y = 0$; (b) and (d) the cross section at $x = 0$.

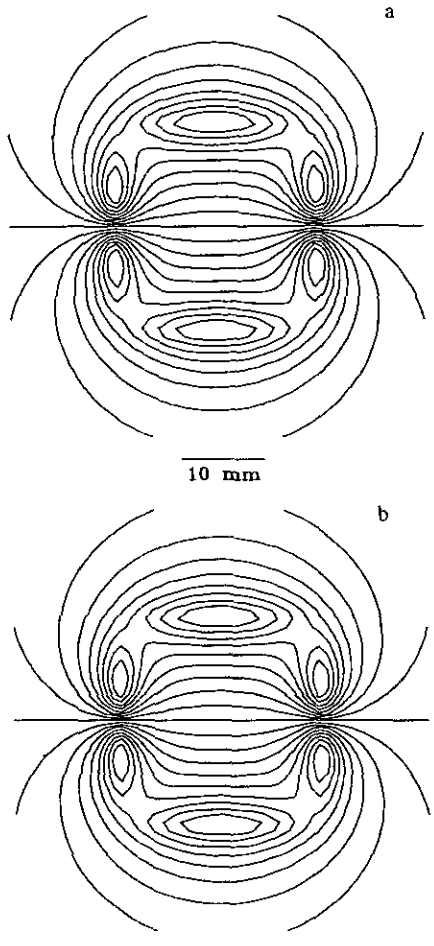

FIG. 15. The magnetic field due to the current on the edge of the conducting plate: (a) The magnetic field due to the contribution of original current on the edge; (b) the magnetic field due to the contribution of the edge of the reconstructed current image (1.3 nT contours).

To verify this formula, we evaluate the line integral of the original current distribution shown in Fig. 11a along the edge to calculate the magnetic field. The corresponding result is shown in Fig. 15a, which is identical, within the numerical precision of the calculation, to the result calculated by the law of Biot-Savart (Fig. 11b).

This observation reveals an approach to characterize the inhomogeneities or the anisotropies in an object from the measured magnetic field data. Since the finite element method can recover current distributions within a bounded region, the current density on the edge of an object is retrievable from the current image. If the object is homogeneous and isotropic, then the results of Eq. (39) should agree with the recorded magnetic field within reasonable accuracy. On the other hand, if the conductivity of the object is either inhomogeneous or anisotropic, the line integral of the computed current along the edge of a homogeneous finite element grid should produce a different magnetic field pattern than the measured one.

We use the reconstructed current (Fig. 13a) to calculate the line integral in Eq. (39). The result shown in Fig. 15b matches the calculated magnetic field (Fig. 11b) perfectly. This confirms that our modeled conducting plate is homogeneous and isotropic because the result of the linear integral of Eq. (39) is equal to the measured magnetic field.

Let us now consider an inhomogeneous 26 mm × 26 mm conducting plate as shown in Fig. 16, whose conductivity (σ_1) in the upper half is twice that (σ_2) in the lower half. If the voltages ($\pm V$) are applied at both sides of the plate as indicated in Fig. 16, then the corresponding Laplace's equation will be

$$\frac{\partial^2 \phi_{1,2}}{\partial x^2} + \frac{\partial^2 \phi_{1,2}}{\partial y^2} = 0, \tag{40}$$

with the boundary conditions of

$$\phi_{1,2} = +V \quad \text{if } x = -a/2 \tag{41}$$

$$\phi_{1,2} = -V \quad \text{if } x = +a/2 \tag{42}$$

$$\frac{\partial \phi_1}{\partial x} = \frac{\partial \phi_2}{\partial x} \quad \text{if } y = 0, \tag{43}$$

where a is the width of the plate. By solving the above equation we find that the associated current distribution in region one ($\mathbf{J}_1$) and region two ($\mathbf{J}_2$) are

$$\mathbf{J}_1 = \frac{2\sigma_1 V}{a}\hat{\imath}$$
$$\mathbf{J}_2 = \frac{2\sigma_2 V}{a}\hat{\imath}. \tag{44}$$

Figure 17a shows the current pattern calculated by Eq. (44) and the corresponding magnetic field is shown in Fig. 17b. Assuming we know the size of the conducting plate, we reconstruct the original current pattern by using the finite element method. The imaging current has a MSD of 0.0024 and is shown in Fig. 17c.

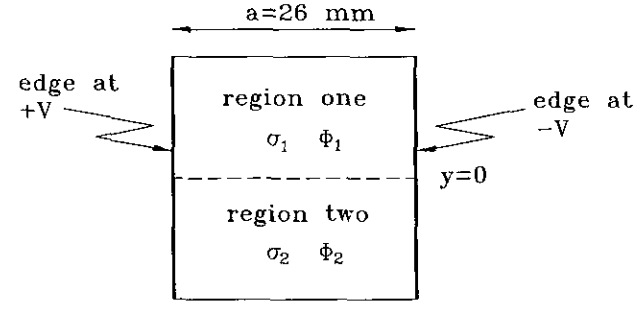

FIG. 16. A schematic representation of the simulated, finite inhomogeneous conducting plate.

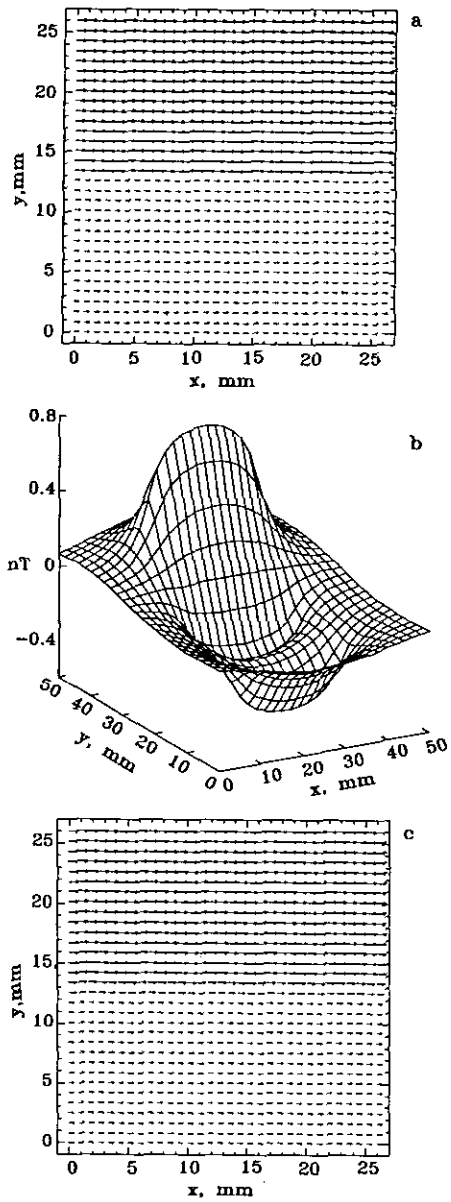

FIG. 17. The forward and inverse calculations for the inhomogeneous conducting plate in Fig. 16: (a) The original current distribution; (b) the associated magnetic field; (c) the reconstructed current pattern.

When we perform the line integral in Eq. (39) for the original current pattern, we find that the magnetic field due to the actual current on the edges (Fig. 18b) is clearly different from the actual magnetic field shown in Fig. 18a. The result of the line integral of Eq. (39) for the reconstructed current pattern (Fig. 18c) also presents these different contours and is in agreement with the image from the line integral. This is clear evidence that for inhomogeneous conducting media, the line integral along the edges will not give the actual magnetic field, while for a homogeneous object it does. We can go one step further and look at the difference between the actual field and that due to the edges, as shown in Fig. 18d. This difference field unambiguously indicates the presence of the internal discontinuity at the middle of the object and suggests that this process can be used to eliminate edge effects while searching for flaws in otherwise homogeneous, bounded objects.

CONCLUSIONS

From these calculations, we conclude that the finite element method is an excellent technique to deconvolve a bounded current source, by constraining the current image within the certain region. Frequently we know the geometry of the object we need to reconstruct. By using this geometry as a constraint condition for the model, we eliminate many uncertain points that would otherwise degrade the inverse solution and, thereby, both improve the resolution and reduce the mean-square deviation of the fitted data from the original data. On the other hand, if we do not utilize this constraint condition, the reconstruction grid will most likely extend beyond the current space. As a result, for the portion of grid outside the current source, the corresponding nodal values are zero, which means there are more zero solutions in Eq. (8) and the ill-conditioned matrix A is more singular. With the aid of prior information about the current sources, we can construct an optimum finite element mesh to reduce the intrinsic singularity in the inverse calculation.

Furthermore, for the current imaging problem, we have additional constraints on the current pattern, such as specific boundary conditions and continuity of current at the current sources and sinks. By using the finite element method, we can incorporate all of these constraints into the current image and, thereby, improve the quality of the image. The finite element method is a general approach that can be used in other inverse imaging techniques and readily allows the inclusion of *a priori* information to minimize the effects of the intrinsic ill-conditioned nature of the inverse imaging problem.

In this analysis, we have used our own implementation of the standard finite element approach [8] to solve the forward problem of calculating the expected current and field distributions for a given sample and current-injection geometry, and we have shown how the finite element equations can be solved using singular value decomposition to provide a constrained finite-element solution to the inverse problem of determining the current distribution from the measured field map given *a priori* knowledge of the sample geometry and electrode configuration. Commercial finite element programs could be readily used for the forward calculations; if such programs provide access to the matrices containing the coefficients for the interpolation functions, our constrained SVD inverse techniques could then be applied. This would offer the possible advantage of allowing the use of more complex mesh geometries than might be attempted with a simple finite element program.

Dependent upon the number of field measurements obtained and the stability of the SVD inverse, it may be possible to

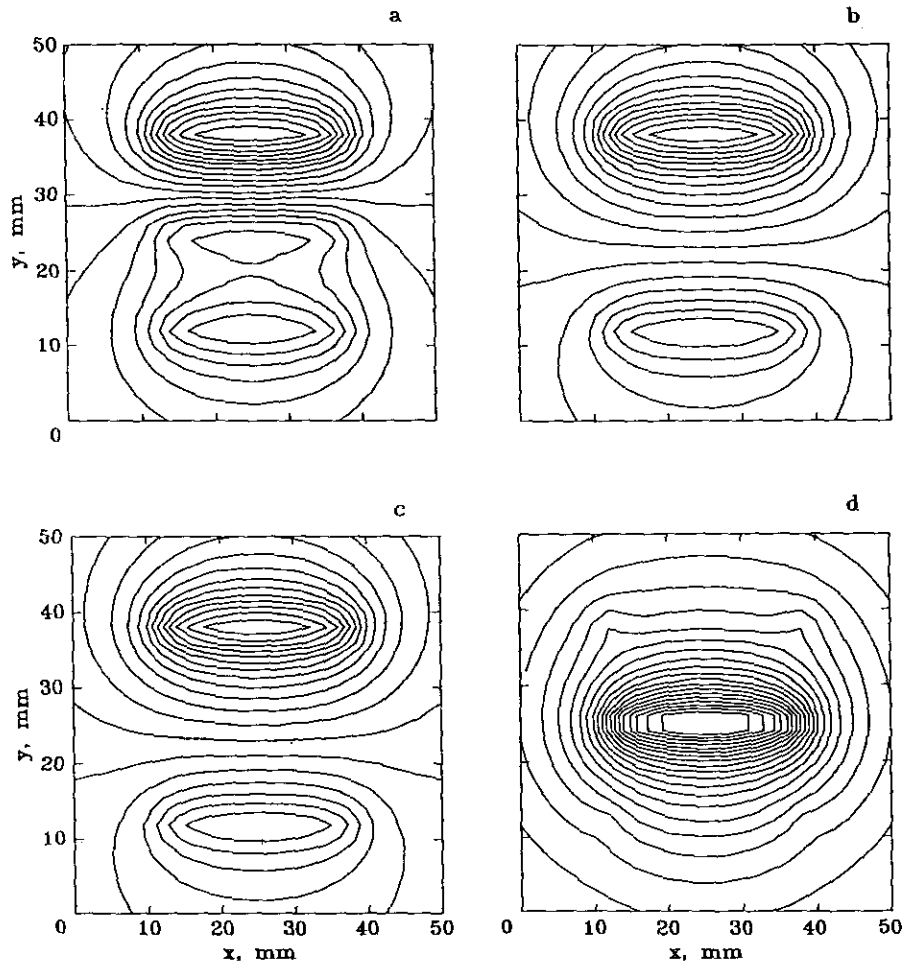

FIG. 18. The comparison of the actual magnetic field and the field due to the current on the edges: (a) the actual magnetic field from Fig. 17b (63 pT contours); (b) the magnetic field due to the original current on the edges (63 pT contours); (c) the magnetic field due to the image current on the edges (63 pT contours); (d) the difference between the actual magnetic field and that due to the image current at the edges (21 pT contours).

extend this approach to nonplanar current distributions. We have also shown [6] that measurements covering only a fraction of the source region can still provide adequate information to reconstruct the entire source distribution, but with reduced accuracy. However, we do not expect that our finite-element inverse approach can be applied to the general, three-dimensional magnetic inverse problem, in which one would like to use measurements of the magnetic field outside the sample to obtain a description of an arbitrary, three-dimensional current distribution within it. Because of the existence of magnetically silent current distributions [11], this problem has no unique solution and it is unlikely that our SVD approach would produce a meaningful solution without additional constraints on the current distribution.

ACKNOWLEDGMENTS

This work has been supported in part by grants from the Air Force Office of Scientific Research and the Electric Power Research Institute. We thank Leonora Wikswo for her comments on the manuscript and Licheng Li for preparing the figures.

REFERENCES

1. J. P. Wikswo, Jr., J. M. Van Egeraat, Y. P. Ma, N. G. Sepulveda, D. J. Staton, S. Tan, and R. S. Wijesinghe, "Instrumentation and Techniques for High-Resolution Magnetic Imaging," in *Digital Image and Synthesis and Inverse Optics*, edited by A. F. Gmitro, P. S. Idell, and I. J. LaHaie, SPIE Proceedings, Vol. 1351 (SPIE, Bellingham, WA, 1990), p. 438.
2. D. J. Staton, R. N. Friedman, and J. P. Wikswo, Jr., *IEEE Trans. Appl. Supercond.* **3**(1), 1934 (1993).
3. B. J. Roth, N. G. Sepulveda, and J. P. Wikswo, Jr., *J. Appl. Phys.* **65**(1), 361 (1989).
4. A. A. Ioannides, J. P. R. Bolton, and C. J. S. Clarke, *Inverse Probl.* **6**, 1 (1990).
5. E. M. Haacke, Z. Liang, and S. H. Izen, *Med Phys.* **16**(3), 388 (1989).
6. S. Tan, Ph.D. dissertation, Department of Physics and Astronomy, Vanderbilt University, Nashville, TN, 1992 (unpublished).

7. W. H. Press, B. P. Flannery, S. A. Teukolsky, and W. T. Vetterling, "Numerical Recipes" (Cambridge Univ. Press, Cambridge, UK, 1986) p. 52.
8. K. Huebner, *The Finite Element Method for Engineers* (Wiley-Interscience, New York, 1975), p. 171.
9. G. Arfken, *Mathematical Methods for Physicists* (Academic Press, New York/London, 1970), p. 758.
10. R. Ilmonieme, "Basic Principles of Biomagnetism," in *Biomagnetic Localization and 3D Modelling*, edited by J. Nenonen and H.-M. Rajala (Otaniemi, 1991).
11. J. P. Wikswo, Jr., "Theoretical Aspects of the ECG–MCG Relationship," in *Biomagnetism: An Interdisciplinary Approach*, edited by S. J. Williamson, G.-L. Romani, L. Kaufman, and I. Modena (Plenum, New York, 1983), p. 311.